

Absorption-selected galaxies trace the low-mass, late-type, star-forming population at $z \sim 2 - 3$

N. H. P. Rhodin^{★1}, J.-K. Krogager², L. Christensen¹, F. Valentino³, K. E. Heintz^{4,3}, P. Møller⁵, T. Zafar⁶, J. P. U. Fynbo³,

¹ DARK, Niels Bohr Institute, University of Copenhagen, Jagtvej 128, DK-2100 Copenhagen Ø, Denmark

² Institut d'Astrophysique de Paris, CNRS-UPMC, UMR7095, 98bis bd Arago, 75014 Paris, France

³ Cosmic Dawn Center (DAWN), Niels Bohr Institute, University of Copenhagen, Jagtvej 128, DK-2100 Copenhagen Ø, Denmark

⁴ Centre for Astrophysics and Cosmology, Science Institute, University of Iceland, Dunhagi 5, 107 Reykjavík, Iceland

⁵ European Southern Observatory, Karl-Schwarzschildstrasse 2, 85748 Garching bei München, Germany

⁶ Australian Astronomical Optics, Macquarie University, 105 Delhi Road, North Ryde, NSW 2113, Australia

Received ; accepted

ABSTRACT

We report on the stellar content, half-light radii and star formation rates of seven new and three known high redshift ($z \gtrsim 2$) galaxies detected as strong neutral hydrogen (H I) absorbers (Damped Ly α Absorbers (DLAs) and sub-DLAs) toward background quasars. We study the their galactic environments, and perform the first systematic morphological characterisation of such absorption-emission pairs at high redshifts. Leveraging the spatial resolution of the Hubble Space Telescope (*HST*) Wide Field Camera 3, and careful Point Spread Function subtraction we image the counterparts of the absorbers in the F606W, F105W, and F160W filters. Our analysis reveals complex, irregular hosts with multiple star-forming clumps. At a drizzled spatial resolution of $0.067 \text{ arcsec pxl}^{-1}$, 40% of our absorption-selected sample requires multiple Sérsic components for an accurate modelling of the observed galaxy light distributions. We measure half-light radii in the range $r_{1/2} \sim 0.4 - 2.6 \text{ kpc}$ based on the reddest band (F160W) to trace the oldest stellar populations, and stellar masses in the range $\log_{10}[M_{\star} (M_{\odot})] \sim 8 - 10$ derived from spectral energy distribution (SED) fits to the broadband *HST* photometry. Spectroscopic- and SED-based star formation rates are largely consistent, and lie in the range $\log_{10}[\text{SFR} (M_{\odot} \text{ yr}^{-1})] = -0.06 - 1.7$. Placed on the mass-size relation and on the main sequence of star forming galaxies, we find that an absorption-selection at high redshift extends known relations determined from deep luminosity-selected surveys to an order of magnitude less massive galaxies, primarily composed of star forming late-types.

Key words: galaxies: evolution — galaxies: photometry — galaxies: stellar content — (galaxies:) quasars: absorption lines

1 INTRODUCTION

Galaxies can be selected via their gas cross-section when there is a chance alignment with a background quasar along the line of sight. In neutral hydrogen (H I), the most H I-rich absorbers are the Damped Lyman- α Absorbers (DLAs; $\log_{10}[\text{N}_{\text{H I}} (\text{cm}^{-2})] \geq 20.3$, Wolfe et al. (1986)) and sub-DLAs ($19.0 \leq \log_{10}[\text{N}_{\text{H I}} (\text{cm}^{-2})] < 20.3$, e.g., Péroux et al. (2003); Zafar et al. (2013)). These classes imprint deep H I absorption lines with characteristic Lorentzian damping wings in the quasar spectrum, and are always accompanied by low-ionisation metal line complexes (Prochaska et al. 2003; Noterdaeme et al. 2012b; Rafelski et al. 2014). Unless otherwise

specified, sub-DLAs and DLAs will collectively be referred to as *strong H I absorbers*.

DLAs alone account for $> 80\%$ of neutral gas out to redshift $z \sim 5$ (Prochaska et al. 2005; Noterdaeme et al. 2012b; Crigton et al. 2015; Sánchez-Ramírez et al. 2016), and combined with the contribution from sub-DLAs, strong H I absorbers efficiently probe the neutral, chemically enriched gaseous environments of galaxies. The connection that strong H I absorbers hold to their harbouring galaxies can be studied by correlating absorption properties with complementary information of the host in emission. Such analysis suggests that absorption-selected galaxies are consistent with the faint end of Lyman-break galaxies (Møller et al. 2002), and that they probe a more representative portion (low mass, faint end of the luminosity function) of galaxy populations across cosmic time than conventional luminosity selections (Fynbo et al.

★ nhp.rhodin@gmail.com

2008; Berry et al. 2016; Krogager et al. 2017). In particular, a recent string of observations indicate that galaxies hosting strong H I absorbers at $z \sim 0.7$ experience suppressed star formation rates (SFR) – either above stellar masses $\log_{10}[M_{\star} (M_{\odot})] \sim 10$ (Rhodin et al. 2018), as a consequence of redshift (Kanekar et al. 2018) or galaxy evolution (Møller et al. 2018). Independent of its cause, a low SFR is remarkable if strong H I absorbers represent the formation-sites for molecular gas and, in extension, reservoirs that maintain star formation.

The current status of how strong H I absorbers relate to their galactic environments hinges on low number-statistics of spectroscopically confirmed absorption-emission pairs. At cosmological redshifts $z \gtrsim 2$, this lack in sample sizes is caused by a combination of low angular separation and an inherent brightness contrast between target galaxy and background quasar; an increased surface brightness dimming with redshift; and the lower mean mass (and therefore luminosity) of galaxies selected by gas cross-section. Indeed, the lack of detections and reported survey statistics are consistent with scaling relation arguments, which suggest that the emission-line targets often fall below detection-limits in blind surveys; whilst pre-selecting on the absorption metallicity yields higher detection rates (Fynbo et al. 2010, 2011) as metal-rich galaxies tend to be more massive, and therefore more luminous (Krogager et al. 2017).

Yet, $z \sim 2 - 3$ allows for simultaneous measurements of the neutral hydrogen column density from the damped Ly α absorption profile and detailed absorption analysis of metal lines with ground-based spectroscopy (Noterdaeme et al. 2012b). This has ensured high fidelity data to base followup campaigns on in search of the counterparts in emission. Indeed, the damped Ly α absorption trough effectively blocks out the quasar light and can be used to search for Ly α emission from the hypothesised host. Owing to the resonance nature of the hydrogen Ly α line, which is known to affect the emerging line-flux from high- z galaxy populations (Verhamme et al. 2008; Laursen et al. 2009; Hayes et al. 2010) and its efficient destruction by dust in more chemically enriched, massive and luminous galaxies (which could mitigate any selection on absorption metallicity), such Ly α searches often resulted in non-detections of absorber counterparts (Fynbo et al. 2011, 2013). However, taking advantage of the large wavelength coverage in modern spectrographs to simultaneously detect strong-rest-frame optical emission lines, ground-based observational efforts have been increasingly successful, most prominently seen in the high detection-rate achieved with the Very Large Telescope (VLT) X-Shooter (VLT/X-Shooter, Vernet et al. 2011) campaign (Fynbo et al. 2010; Krogager et al. 2017).

Whereas spectroscopic searches for galaxy counterparts in the past primarily focused on identifying the correct host, analyses of the emission originating from their stellar components have typically been reported as individual case studies (Møller et al. 2002; Fynbo et al. 2013; Krogager et al. 2013; Augustin et al. 2018). Even though we have assembled a significant sample of $z \gtrsim 2$ DLA-galaxy pairs, a comprehensive investigation of the stellar contents of the galaxies as a population is lacking. Here, we take advantage of the detailed information available from ground-based spectra to search for the counterparts of strong H I absorbers at $z \sim 2 - 3$ with multi-band photometric Hubble Space Telescope (*HST*) imaging. With its exquisite spatial resolution and in absence of the telluric atmosphere, *HST* allows us to disentangle the emission from the intervening galaxy and background quasar and, thereby, determine stellar masses and morphologies. This directly addresses the low-number statistics; enables scaling relations at high- z to be explored

independent of samples at low redshift; and allows the low-mass extensions of any relations established from luminosity-selected galaxy samples to be probed.

The paper is organised as follows: Section 2 describes sample selection, observations, and data-reduction; Section 3 presents our imaging, photometry, morphological analysis, and spectral energy distribution (SED) based stellar mass measurements; and Section 4 places our findings in context with known high-redshift galaxy scaling relations. In Section 5 we summarise our conclusions. Throughout this paper, we assume a flat Λ cold dark matter (Λ CDM) cosmology, with $H_0 = 70.4 \text{ km s}^{-1} \text{ Mpc}^{-1}$ and $\Omega_{\Lambda} = 0.727$ (Komatsu et al. 2011) to ensure consistency with prior work (e.g. Christensen et al. 2014; Møller et al. 2018; Rhodin et al. 2018). Magnitudes are reported in the AB magnitude system. Star formation rates are derived on a Chabrier (2003) initial mass function (IMF). To quantify the degree of consistency between two measurements, $\mu_1 \pm \sigma_1$ and $\mu_2 \pm \sigma_2$, we report the number of sigmas statistical tension as $|\mu_1 - \mu_2| / \sqrt{\sigma_1^2 + \sigma_2^2}$.

2 OBSERVATIONS AND DATA-REDUCTION

2.1 Sample selection

We select targets to study morphology and stellar mass content in high redshift ($z \gtrsim 2$) absorption-selected galaxies with *HST* imaging (see Section 2.2). To break model degeneracies with only three broad-band magnitudes we require each target to have a spectroscopically confirmed redshift, determined from emission lines at z_{abs} and measured in the quasar spectrum (see Table 2 for individual entry references). In addition, spectroscopic redshifts and high spatial resolution allows accurate conversions of angular separations to physical distances, and therefore measurements of the projected spatial scales that connect the emission and absorption.

A large fraction of the confirmed hosts were originally selected on the absorption properties in intermediate resolution X-Shooter quasar spectra (for an overview of the X-Shooter observing strategy, see Krogager et al. 2017). These absorbers were, themselves, selected from their high Si II $\lambda 1526\text{\AA}$ rest-frame equivalent widths as measured in Sloan Digital Sky Survey (SDSS, Richards et al. 2001; Noterdaeme et al. 2009a) spectra since the Si II $\lambda 1526\text{\AA}$ line acts as a proxy for high metallicity absorbers (Prochaska et al. 2008) – and therefore are more likely to be hosted by luminous counterparts (Fynbo et al. 2010, 2011; Krogager et al. 2012; Noterdaeme et al. 2012a; Péroux et al. 2012; Bouché et al. 2013; Fynbo et al. 2013; Krogager et al. 2013; Rahmani et al. 2016; Rhodin et al. 2018).

In summary then, our sample consists of seven new and three re-analysed $z_{\text{abs}} \sim 1.8 - 3.1$ spectroscopically confirmed galaxies hosting a total of eight DLAs and two sub-DLAs in 10 quasar fields, with a sample selection biased towards high-metallicity absorbers.

2.2 HST data

To study stellar content and morphology, we acquired *HST* broad-band images in Wide Field Camera 3 (WFC3) using the Ultraviolet-Visible (UVIS) channel UVIS/F606W, and the Infrared (IR) channel IR/F105W and IR/F160W filters (new detections: Cycle 23, ID 14122, PI. Christensen; re-analysed detections: Cycle 19, ID 12553, PI. Fynbo). At the targets' redshifts, this allowed us to map their stellar continuum around the rest-frame Balmer jump. Each target was imaged with one orbit per filter (except Q 0338–0005 which

Quasar Field	R.A. [J2000] [hh:mm:ss]	Dec. [J2000] [° : ' : "]	$N_{\text{orb}} \times N_{\text{exp}} \times t_{\text{exp}}$		
			UVIS/F606W [s]	IR/F105W [s]	IR/F160W [s]
Q0124+0044	01:24:03.78	+00:44:32.74	$1 \times 4 \times 621$	$1 \times 4 \times 653$	$1 \times 4 \times 653$
Q0139-0824	01:39:01.41	-08:24:44.05	$1 \times 4 \times 622$	$1 \times 4 \times 653$	$1 \times 4 \times 653$
Q0310+0055	03:10:36.85	+00:55:21.66	-	$1 \times 4 \times 653$	$1 \times 4 \times 653$
Q1313+1441	13:13:41.20	+14:41:40.60	$1 \times 4 \times 623$	$1 \times 4 \times 653$	$1 \times 4 \times 653$
Q2059-0528	20:59:22.43	-05:28:42.78	$1 \times 4 \times 622$	$1 \times 4 \times 653$	$1 \times 4 \times 653$
Q2239-2949	22:39:41.77	-29:49:54.47	$1 \times 4 \times 626$	$1 \times 4 \times 653$	$1 \times 4 \times 653$
Q2247-6015	22:47:08.93	-60:15:45.30	$1 \times 4 \times 646$	$1 \times 4 \times 703$	$1 \times 4 \times 703$
Q0338-0005	03:38:54.78	-00:05:21.01	$2 \times 4 \times 627$	-	-
Q2222-0946	22:22:56.11	-09:46:36.29	$1 \times 4 \times 629$	$1 \times 4 \times 653$	$1 \times 4 \times 653$
Q0918+1636	09:18:26.16	+16:36:09.02	$1 \times 4 \times 631$	$1 \times 4 \times 653$	$1 \times 4 \times 653$

Table 1. Observation log for the *HST* imaging. R.A. and Dec. refer to the coordinates of the quasar, taken from the SIMBAD database (Wenger et al. 2000). N_{orb} refers to the number of orbits; N_{exp} to the number of exposures; and t_{exp} to the exposure time of an individual exposure in units of seconds.

Quasar Field	z_{QSO}	z_{abs}	$\log_{10}(N_{\text{HI}})$ [$\log_{10}(\text{cm}^{-2})$]	Tracer	$[M/H]_{\text{abs}}$ [dex]	θ [arcsec]	b [kpc]	SFR [$M_{\odot} \text{ yr}^{-1}$]
Q0124+0044	3.84	2.2616 ^(j)	$20.70 \pm 0.15^{(j)}$	Zn II	$-0.67 \pm 0.16^{(j,s)}$	1.3	10.9	$> 0.1^{(k)}$
Q0139-0824	3.01	2.6773 ^(f)	$20.70 \pm 0.15^{(f)}$	Si II	$-1.24 \pm 0.20^{(k)}$	1.6	13.0	$> 0.7^{(k)}$
Q0310+0055	3.78	3.1150 ^(a)	$20.05 \pm 0.05^{(a)}$	-	-	3.8 ^(a)	29.6 ^(a)	$0.54 \pm 0.0_{\text{Ly}\alpha}^{(a)}$
Q1313+1441	1.89	1.7941 ^(e)	$21.30 \pm 0.10^{(e)}$	Zn II	$-0.86 \pm 0.14^{(e,s)}$	1.3 ^(e)	11.3 ^(e)	$> 0.3_{\text{Ly}\alpha}^{(e)}$
Q2059-0528	2.54	2.2101 ^(b)	$21.00 \pm 0.05^{(b)}$	Zn II	$-0.96 \pm 0.06^{(b)}$	$< 0.8^{(b)}$	$< 6.3^{(b)}$	$0.2_{\text{Ly}\alpha}^{(b,e)} < \text{SFR} < 1.4_{\text{H}\alpha}^{(l)}$
Q2239-2949	2.10	1.8250 ^(h,i)	$19.84 \pm 0.14^{(g)}$	Si II	$-0.67 \pm 0.15^{(g)}$	2.4 ^(g)	20.8 ^(g)	$0.07 \pm 0.01_{\text{Ly}\alpha}^{(g)}$
Q2247-6015	3.01	2.3288 ^(c,d)	$20.62 \pm 0.05^{(c)}$	Zn II	$-0.91 \pm 0.05^{(m,s)}$	3.1 ^(c,m)	26 ^(c,m)	$33^{+40}_{-11} \text{H}\alpha^{(m)}$
Q0338-0005	3.05	2.2298 ⁽ⁿ⁾	$21.09 \pm 0.10^{(n)}$	Si II	$-1.37 \pm 0.06^{(e,s)}$	0.49 ^(o)	4.1 ^(o)	$> 0.3_{\text{H}\alpha}^{(e)}$
Q2222-0946	2.93	2.35409 ⁽ⁿ⁾	$20.65 \pm 0.05^{(p)}$	Zn II	$-0.53 \pm 0.07^{(p)}$	0.80 ^(p,s)	6.7 ^(p)	$13 \pm 1_{\text{H}\alpha}^{(e)}$
Q0918+1636	3.09	2.5832 ^(q)	$20.96 \pm 0.05^{(q)}$	Zn II	$-0.19 \pm 0.05^{(p,s)}$	2.0 ^(r)	16.4 ^(r)	$8 \pm 3_{\text{H}\alpha}^{(r)}$

Table 2. Archival data for the targeted strong H I absorbers and their host galaxies. Spectroscopic quasar redshifts (z_{QSO}) are taken from the SIMBAD database. None of our targets are proximate absorbers ($\Delta v_{\text{QSO-abs}} < 5000 \text{ km s}^{-1}$). The spectroscopically identified hosts have positions relative to the quasars hosting the absorption, measured as projected separations (θ , in arcsec) and impact parameters (b , in kpc). All SFRs are reported for a Chabrier IMF. Super-scripts give references to individual entries. Sub-scripts refer to the spectral line on which the SFR was inferred. For Q0124+0044 and Q0139-0824 the impact parameters and SFRs refer to those derived from the new identifications published in this work (see Sections 2.3.1 and 2.3.2, respectively). For Q0139-0824, we report the metallicity based on the absorption analysis performed in this work (see Section 3.1). References: ^(a)Kashikawa et al. (2014), ^(b)Hartoog et al. (2015), ^(c)Bouché et al. (2012), ^(d)Lopez et al. (2002), ^(e)Krogager et al. (2017), ^(f)Wolfe et al. (2008), ^(g)Zafar et al. (2017), ^(h)Cappetta et al. (2010), ⁽ⁱ⁾Zafar et al. (2013), ^(j)Berg et al. (2016), ^(k)This work, ^(l)Péroux et al. (2012), ^(m)Bouché et al. (2013), ⁽ⁿ⁾Bashir et al. (2019), ^(o)Krogager et al. (2012), ^(p)Fynbo et al. (2010), ^(q)Fynbo et al. (2011), ^(r)Fynbo et al. (2013), ^(s)Møller & Christensen (2020).

was observed with two orbits in F606W), subdivided into four exposures of equal lengths. We used a standard four-point dither pointing strategy designed to provide an optimal subpixel point-spread function (PSF) sampling (WFC3-UVIS-DITHER-BOX and WFC3-IR-DITHER-BOX-MIN patterns in the F606W, and the F105W- and F160W filters, respectively). The orientation (impact parameters and position-angles) of the galaxies relative to the quasars responsible for the absorption were known from long-slit quasar spectra. This allowed us to optimise the positioning of the diffraction spikes and avoid detector bleeding effects. The observation log is summarised in Table 1.

To reduce individual exposures we ran a standard AstroDrizzle processing pipeline based on the Python DrizzlePac¹. For a detailed description of AstroDrizzle, we refer to the STScI DrizzlePac documentation. With the Object

Association (ASN) Table, this procedure constructs a parameter file which was used to align frames and perform sky subtraction and cosmic ray rejection. Individual exposures in each filter and for each object were drizzled into final, inverse variance (IVM) weighted science frames. For each filter, we selected combinations [final_pixfrac, final_scale (arcsec/pxl)]_{filter} of [0.7, 0.024]_{F606W}; [0.7, 0.066]_{F105W}; and [0.7, 0.066]_{F160W}. These values allowed us to recover a high spatial resolution in the drizzled images and ensured partial pixel-overlap to avoid image fragmentation. In addition, identical drizzle settings for all objects in a given filter allows us to construct empirical, non-parametric PSFs based on the quasars (see Section 3.2).

2.3 Archival data

In this Section, we review the relevant archival data extracted for individual quasar fields. For consistency, we standardise all star formation rates to a Chabrier IMF. Literature values based on a Salpeter IMF are converted to their Chabrier IMF equivalents by applying a

¹ DrizzlePac is a product of the Space Telescope Science Institute (STScI), designed as a set of callable modules which can also be run as a single task: AstroDrizzle.

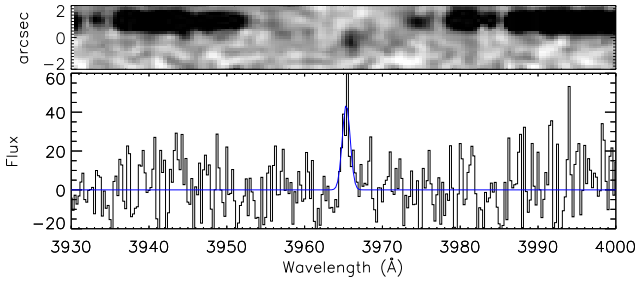


Figure 1. Section of the 2-dimensional X-shooter spectrum around the damped $\text{Ly}\alpha$ line towards Q 0124+0044. The 2D spectrum has been smoothed by a Gaussian function with a FWHM of 3 pixels. At an impact parameter of ~ 1.3 arcsec from the quasar, $\text{Ly}\alpha$ emission is detected from the host galaxy of the DLA system. The best fit Gaussian function is overlaid on the 1D spectrum.

downwards correction factor of 1.8. For objects solely detected in $\text{Ly}\alpha$, we have implicitly assumed standard Case B recombination theory ($f_{\text{Ly}\alpha}/f_{\text{H}\alpha} = 8.7$) and escape fractions of unity to convert a $\text{Ly}\alpha$ flux to the Kennicutt (1998) $\text{H}\alpha$ -based star formation rate estimator. For a summary of the quantities, we refer the reader to Table 2.

2.3.1 Q 0124+0044

This quasar was targeted in the large X-shooter legacy sample XQ-100 (López et al. 2016, Programme ID 189.A-0424). Having one of the most metal-rich DLAs in that sample (Berg et al. 2016), the X-shooter slit was placed at a single position angle at +130 deg East of North that serendipitously contained emission from the DLA host. In the 2-dimensional spectrum we detected emission lines from $\text{Ly}\alpha$ and $[\text{O III}] \lambda 5007 \text{ \AA}$ offset spatially by 1.0–1.3 arcsec from the quasar trace. The $\text{Ly}\alpha$ emission is illustrated in Figure 1. Extinction corrections from the extinction maps of Schlafly & Finkbeiner (2011) are applied as follows, $A_{\text{F606W}} = 0.071$, $A_{\text{F105W}} = 0.022$ and $A_{\text{F160W}} = 0.014$ magnitudes. Integrating the line gives a line flux of $f(\text{Ly}\alpha) = (5.8 \pm 0.3) \times 10^{-18} \text{ erg cm}^{-2} \text{ s}^{-1}$ at $z_{\text{em}} = 2.2617$ after correction for Galactic reddening, and suggests a lower limit for the star-formation rate of $0.1 \text{ M}_{\odot} \text{ yr}^{-1}$ based on a Chabrier IMF.

2.3.2 Q 0139–0824

A tentative detection of $\text{Ly}\alpha$ emission was originally seen in VLT Visible Multi-Object Spectrograph (VLT/VIMOS, Le Fèvre et al. 2003) IFU data. Follow-up deeper observations with the VLT Focal Reducer and low dispersion Spectrograph (VLT/FORS1, Appenzeller et al. 1998) in Aug. and Sep. 2008 (Programme ID 081.A-0506) provided the proof of a detection of $\text{Ly}\alpha$ offset by ~ 1.6 arcsec to the South-West from the trace of the quasar as illustrated in Figure 2. During X-shooter observations aimed to identify additional emission lines besides $\text{Ly}\alpha$ (Programme ID 088.A-0378) the recorded seeing measured from the quasar PSF was 1.4–1.5 arcsec, and the chosen slit width of 1.2 arcsec was placed at position angle of -98 deg. East of North. No additional emission lines were detected corresponding to the DLA redshift, but at the redshift of the DLA, all other strong optical emission lines are severely affected by telluric absorption. We note that the slit position angles used for spectroscopy do not correspond exactly to the position angle of the

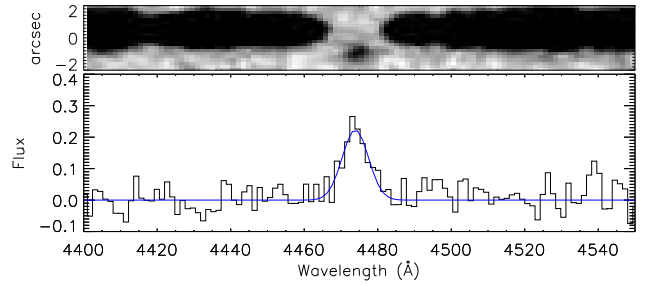


Figure 2. Section of the 2-dimensional FORS1 spectrum around the damped $\text{Ly}\alpha$ line towards Q 0139–0824. The spectrum has been smoothed by a Gaussian function with a FWHM of 2 pixels. At an impact parameter of ~ 1.6 arcsec from the quasar, $\text{Ly}\alpha$ emission is detected from the host galaxy. The best fit Gaussian function is overlaid on the 1D spectrum.

galaxy measured directly in the *HST* images, as we did not at that time have sufficient spatial information to optimally orient the slit.

We adopt extinction correction factors at the position of the quasar, with retrieved values of $A_{\text{F606W}} = 0.068$, $A_{\text{F105W}} = 0.022$ and $A_{\text{F160W}} = 0.014$ magnitudes. Integrating the $\text{Ly}\alpha$ line gives a line flux of $f(\text{Ly}\alpha) = (2.2 \pm 0.2) \times 10^{-17} \text{ erg cm}^{-2} \text{ s}^{-1}$ at $z_{\text{em}} = 2.6791$ after correcting for Galactic extinction, and suggests a lower limit for the SFR of $0.7 \text{ M}_{\odot} \text{ yr}^{-1}$ based on a Chabrier IMF.

2.3.3 Q 0310+0055

The absorbing galaxy in the Q 0310+0055 field was confirmed as host with Subaru Faint Object Camera and Spectrograph (Subaru/FOCAS, Kashikawa et al. 2002) long-slit spectra (Kashikawa et al. 2014). With a 0.8 arcsec slit-width and a varying seeing of the order 0.5 - 1.0 arcsec, their observations may suffer from significant slit-losses. No dust-extinction- or slit-loss corrections were applied. The reported impact parameter is based on the peak position of extended $\text{Ly}\alpha$ emission.

We note that our PSF subtracted fields reveal two objects at lower impact parameters (blue circular apertures, see Figure 5). However, Kashikawa et al. (2014) do not detect $\text{Ly}\alpha$ emission at the absorber redshift at lower impact parameters. Since evidence for a physical connection is absent, we therefore disregard them in the remainder of this work, but note that the detections may be related objects which do not emit in $\text{Ly}\alpha$. Further investigation of the field must be done to reveal the nature of these objects. To accommodate the Subaru/FOCAS NB502 narrow-band detection ($\text{mag}_{\text{NB502}} = 25.46 \pm 0.13$) (Kashikawa et al. 2014) in our stellar mass analysis (see Section 3.4), we first remove the contribution from $\text{Ly}\alpha$ nebulae emission. Based on a reported $\text{Ly}\alpha$ luminosity of $L_{\text{Ly}\alpha} = 1.07 \pm 0.14 \times 10^{42} \text{ ergs s}^{-1}$, and assuming a flat spectral shape over NB502, with a filter width of 60 Å, we solve for a NB continuum magnitude of $\text{NB502}_{\text{cont.}} = 26.8 \pm 0.6$. For the SED fits with LePhare (see Section 3.4), we then construct a simple box-shaped narrow-band filter transmission curve with a central wavelength $\lambda_c = 5025 \text{ \AA}$ and a width of 60 Å, based on the filter specification outlined on the Subaru homepage.² We also include their *B*- and *V*-band non-detections (25.32 and 25.50 magnitudes, respectively) reported as the 3σ limiting magnitudes in 2 arcsec apertures at the position of the narrow-band detection. Finally, all

² <https://www.naoj.org/Observing/Instruments/FOCAS/camera/filters.html>

magnitudes (measurements and limits) are corrected for Galactic extinction prior to entering the LePhare setup. Individual values are as follows: $A_B = 0.414$, $A_{NB502} = 0.343$, $A_V = 0.305$, $A_{F105W} = 0.082$, $A_{F160W} = 0.052$.

2.3.4 Q 1313+1441

The galaxy host of the absorber in Q 1313+1441 was confirmed by Krogager et al. (2017) based on Ly α emission in the trough of the damped Ly α absorption profile. The authors report an impact parameter based on X-Shooter slit-spectra triangulation. The Ly α measurement may suffer from slit-losses and dust-extinction, which is why the star formation rate is presented as a conservative lower limit. Based on detections in different slit positions, Krogager et al. (2017), suggest that the emission arise in a galaxy group environment. We adopt extinction correction factors at the position of the quasar, with retrieved values of $A_{F606W} = 0.051$, $A_{F105W} = 0.016$ and $A_{F160W} = 0.010$ magnitudes.

2.3.5 Q 2059–0528

This object was observed by Hartoog et al. (2015), following the 3 slit position angle observational strategy of other X-Shooter campaigns (Fynbo et al. 2010; Krogager et al. 2017). This allowed simultaneous measurements in absorption and emission. Emission was detected at all position angles, suggesting an object at low impact parameter (< 0.75 arcsec, corresponding to an impact parameter of < 6.3 kpc) in the overlapping spectral region. With Ly α detections in all slit positions, the slit triangulation only yields an upper limit on the impact parameter. A 3σ detection of Ly α in emission at the trough of the damped Ly α absorption profile is found in a stacked spectrum. Converting the Ly α measurement to H α gives a lower bound on the SFR. The measurement may suffer from slit-losses and dust-extinction. The 1D quasar spectrum follows the shape of a dereddened composite quasar spectrum (Vanden Berk et al. 2001), hence the continuum extinction is not significant along the quasar line-of-sight. That does not exclude that the galaxy counterpart by itself could have an amount of dust that affects the detected emission lines. Péroux et al. (2012) used SINFONI IFU observations to search the quasar field for the host galaxy in H α emission. This yielded an H α non-detection, which translates into a robust upper limit on the SFR. We adopt extinction correction factors of $A_{F606W} = 0.104$, $A_{F105W} = 0.033$, and $A_{F160W} = 0.021$ magnitudes.

2.3.6 Q 2239–2949

The absorber in quasar field Q 2239–2949 (Zafar et al. 2013; Zafar et al. 2013) and its host were investigated by Zafar et al. (2017). The absorber is a sub-DLA, and no ionisation corrections were applied for its reported metallicity. However, the authors report an [Si/Fe] ratio, which suggests that a combination of ionisation and dust effects are present. Observations reveal Ly α in emission at z_{abs} , offset from the spatial position of the absorber by an impact parameter measured from X-Shooter slit triangulation. Converting the Ly α measurement to H α gives a dust-uncorrected SFR with propagated flux-measurement errors, as reported in Table 2. Based on slit width and seeing, the authors quantify the slit-loss corrections to be less than a factor of 2. With a maximum correction factor of 20 to account for both dust and slit losses, they estimate an upper limit on the SFR of $\sim 1.4 M_{\odot} \text{ yr}^{-1}$. We adopt extinction correction

factors of $A_{F606W} = 0.043$, $A_{F105W} = 0.013$, and $A_{F160W} = 0.009$ magnitudes.

2.3.7 Q 2247–6015

This quasar absorber was first analysed by Lopez et al. (2002) with a high S/N, high resolution UVES spectrum. Bouché et al. (2012, 2013) conducted comprehensive followup observations of the quasar field (alternative name; HE 2243–60) to look for the absorbing galaxy in emission using SINFONI IFU data. Not affected by slit-losses, the authors reported a dust-corrected H α star formation rate. Their analysis also included a re-analysis of the absorber, combining archival observations to achieve deeper observations. We therefore choose to report emission and absorption properties based on Bouché et al. (2012, 2013). We adopt extinction correction factors of $A_{F606W} = 0.047$, $A_{F105W} = 0.015$, and $A_{F160W} = 0.009$ magnitudes.

2.3.8 Q 0338–0005

This quasar has a DLA and a sub-DLA reported along its line of sight (Zafar et al. 2013). Previously, Noterdaeme et al. (2009b) reported the H I column density of both absorbers and Bashir et al. (2019) re-determined the column densities using the high resolution UVES spectrum. The Ly α emission from the DLA host-galaxy was reported by Krogager et al. (2012) and was confirmed in the UVES spectrum by Bashir et al. (2019). Krogager et al. (2012) reported the galaxy at an impact parameter of $b = 0.49 \pm 0.13$ arcsec. From the measured Ly α flux of $f(\text{Ly}\alpha) = (1.3 \pm 0.2) \times 10^{-17} \text{ erg s}^{-1} \text{ cm}^{-2}$, Krogager et al. (2017) reported a lower limit of $\text{SFR}(\text{Ly}\alpha) > 0.3 M_{\odot} \text{ yr}^{-1}$. In Figure 3 we illustrate a tentative candidate counterpart detection, which is only visible after subtraction of the PSF, located 0.39 ± 0.02 arcsec from the quasar line of sight.

2.3.9 Q 2222–0946

The absorber towards Q 2222–0946 was reported by Noterdaeme et al. (2009a) and its host galaxy was detected by Fynbo et al. (2010) using the X-shooter triangulation strategy. The DLA was found to be at an impact parameter of 0.8 ± 0.1 arcsec (6 kpc at $z_{\text{abs}} = 2.354$), at a predicted position angle of 40 deg based on X-shooter slit triangulation. This was confirmed by Krogager et al. (2013) who identified the target at an impact parameter of 0.74 arcsec corresponding to 6.3 kpc at $z = 2.354$ at PA = 26.45 deg East of North. Ly α , [O II], [O III], and H α emission lines have been detected in X-shooter spectra (Fynbo et al. 2010) and Keck/Osiris data (Jorgenson & Wolfe 2014). The SFR based on H α is calculated to be $13 \pm 1 M_{\odot} \text{ yr}^{-1}$ (Krogager et al. 2017). For the F606W, F105W and F160W magnitudes we adopt extinction correction factors of 0.103, 0.032 and 0.021 magnitudes, respectively.

2.3.10 Q 0918+1636

The quasar absorber in emission was detected with the X-shooter metal-rich DLA triangulation strategy method (Fynbo et al. 2011). Fynbo et al. (2011) reported emission from [O II] and [O III] and H $_2$ molecules in absorption are also detected. Later, Fynbo et al. (2013) detected H α and H β emission lines and using the HST data, performed the SED fit. Fynbo et al. (2013) find the DLA galaxy

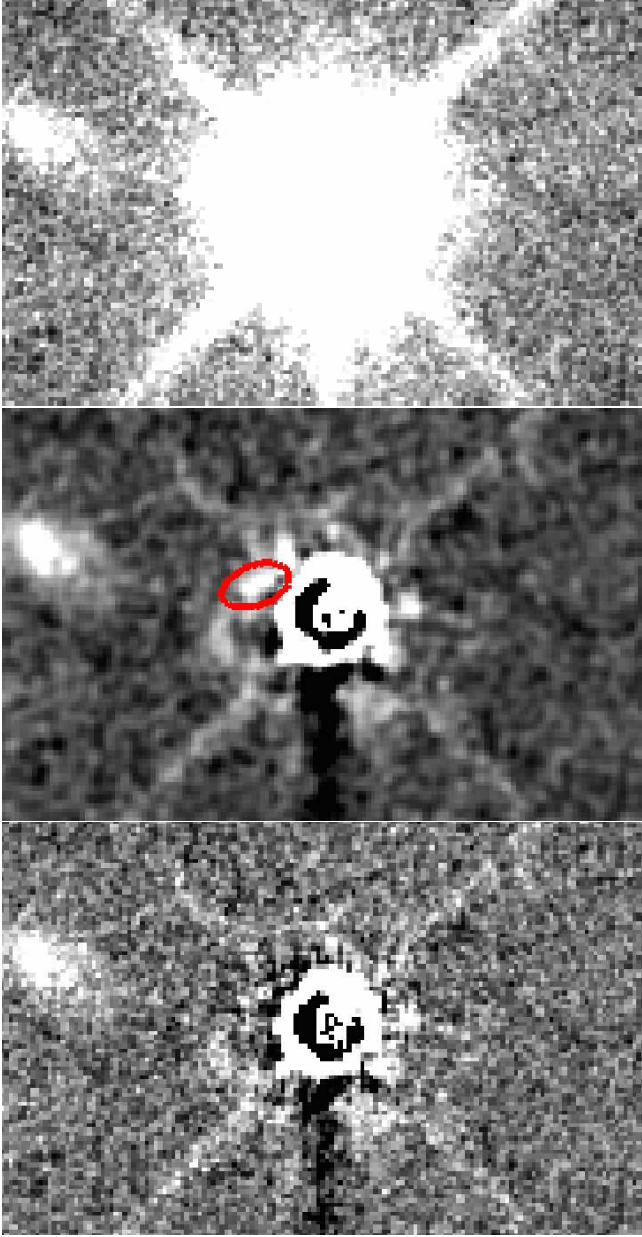


Figure 3. Tentative counterpart detection in the Q0338-0005 field. *Top:* A zoom-in of the quasar vicinity. *Centre:* Quasar PSF subtracted residuals, revealing tentative counterpart (red ellipsoid) at low projected separation. *Bottom:* Residual image after simultaneous fitting of quasar PSF and tentative DLA galaxy counterpart.

associated with the $z_{\text{abs}} = 2.583$ absorber at an impact parameter of 1.98 ± 0.02 arcsec from quasar (proper distance of 16.2 kpc), at a position angle of -115 deg East of North. We confirm their finding. The second absorber at $z_{\text{abs}} = 2.412$, has a candidate counterpart located at a position angle of ~ 130 deg East of North, at an impact parameter consistent with zero, with a conservative upper limit of 0.25 arcsec corresponding to 2.0 kpc, based on detections of Ly α and [O III] $\lambda 5007$ in a co-added 2D spectrum. We cannot confirm such an object with our quasar point spread function (qPSF) subtraction technique as detailed in Section 3.2. In addition to the re-reduced *HST* images and their associated magnitudes, we also include the SDSS u , g and Nordic Optical Telescope

NOTCam (Abbott et al. 2000) NOTCam/ K_s band photometry reported in Fynbo et al. (2013), which have already been corrected for Galactic extinction. We also apply Galactic extinction corrections to the *HST* magnitudes based on the Schlafly & Finkbeiner (2011) re-calibrated extinction maps at the position of the quasar. For the F606W, F105W and F160W magnitudes we adopt extinction correction factors of 0.058, 0.018 and 0.012 magnitudes, respectively.

3 RESULTS

3.1 Absorption analysis of the Q0139-0824 DLA

The DLA Q0139-0824 has a reported absorption metallicity of $[\text{Si}/\text{H}]_{\text{abs}} = -1.15 \pm 0.15$ dex (Krogager et al. 2012; Hartoog et al. 2015). This value emerged based on unpublished measurements, whereas an extensive literature search only returned a published iron abundance $[\text{Fe}/\text{H}]_{\text{abs}} = -1.62 \pm 0.02$, and a minimally depleted metallicity of $[\text{M}/\text{H}]_{\text{abs}} = -1.27 \pm 0.19$, with respect to solar (Wolfe et al. 2008). Despite marginally consistent measurements to within their respective uncertainties, the discrepancy warrants a re-examination to test whether the difference is systematic or driven by the uncertainties. We therefore use existing X-shooter (Vernet et al. 2011) data (programme ID 088.A-0378; PI: Christensen) and perform our own absorption analysis to determine the gas-phase abundance independently.

The quasar was observed with X-Shooter on 7. Jan 2012 with an integration time of 2×1800 s on target, with the target nodded along the slit. Slit widths of 1.3 arcsec and 1.2 arcsec were chosen for the UVB and VIS+NIR arms, respectively. The data were reduced using standard X-Shooter `esorex` scripts version 2.9.3 (Modigliani et al. 2010), and flux calibrated using observations of the spectrophotometric standard star, Feige 110, observed on the same night. Data from the UVB and VIS arms were reduced in stare mode, and 1D spectra were optimally extracted using custom routines and combined by weighting each spectrum with the average signal to noise ratio. To compute an accurate value for the instrument resolution, even though seeing during the observations was larger than the slit width, we measured spectral resolutions from telluric absorption lines in the quasar spectra to be $\mathcal{R}_{\text{VIS}} = 42 \text{ km s}^{-1}$ and $\mathcal{R}_{\text{NIR}} = 70 \text{ km s}^{-1}$. With a lack of telluric absorption features in the UVB arm, we scale its nominal resolution to the ratio of observed-to-nominal resolution in the visual arm, giving $\mathcal{R}_{\text{UVB}} = 70 \text{ km s}^{-1}$, roughly consistent with $R = 4100$ reported for X-shooters UVB arm at a slit width of 1.3 arcsec (Vernet et al. 2011).

To measure the gas-phase metallicity of the absorber, we fit Voigt profiles to each velocity component of well-defined low-ionisation absorption lines free of telluric contamination in the reduced 1D spectra. We use the python package VOIGTFIT (Krogager 2018), which uses line-lists with updated oscillator strengths (Cashman et al. 2017), and has the added advantage of fitting the continuum together with the line parameters. We select a Chebyshev polynomial of order two as the continuum function, which is fitted around the spectral region covering each line transition.

At the modest spectral resolution, we cannot resolve intrinsically narrow components originating in individual clouds and which may cause line asymmetries. We therefore resort to fit the resolved profile with a conservative two-component velocity structure after binning the spectrum by a factor of two (see Figure 4). We fit all lines simultaneously, tying the broadening-parameter and the redshift for each velocity component. Column densities for

Complex $\lambda = [\text{\AA}]$, $v = [\text{km s}^{-1}]$	b [km s^{-1}]	$\log_{10} [N (\text{cm}^{-2})]$
Al II $\lambda 1670$		
$v_1 = 0 \pm 1$	32 ± 2	13.40 ± 0.06
$v_2 = 104 \pm 2$	11 ± 1	13.85 ± 0.40
Total Column:		13.99 ± 0.29
Fe II $\lambda \lambda 1608, 2344, 2374, 2382$		
$v_1 = 0 \pm 1$	32 ± 2	14.51 ± 0.03
$v_2 = 104 \pm 2$	11 ± 1	14.39 ± 0.07
Total Column:		14.76 ± 0.04
Si II $\lambda \lambda 1526, 1808$		
$v_1 = 0 \pm 1$	32 ± 2	14.71 ± 0.14
$v_2 = 104 \pm 2$	11 ± 1	14.59 ± 0.20
Total Column:		14.97 ± 0.12

Table 3. Absorption analysis of the low-ionisation line-complexes associated with the Q0139-0824 DLA at $z_{\text{sys}} = 2.6775$.

each velocity component and the total ion column are reported in Table 3. We also derive a neutral hydrogen column density consistent with the results presented in Wolfe et al. (2008). We, therefore, fix the neutral hydrogen column density to the reported value $\log_{10} [N_{\text{H I}} (\text{cm}^{-2})] = 20.70 \pm 0.15$ and measure gas-phase metallicities of $[\text{Al}/\text{H}] = -1.16 \pm 0.33$, $[\text{Si}/\text{H}] = -1.24 \pm 0.20$ and $[\text{Fe}/\text{H}] = -1.44 \pm 0.16$ with respect to the solar photosphere elemental abundances in Asplund et al. (2009).

Less refractory elements such as S and Zn are less depleted onto dust grains and are thus more suitable tracers of the gas-phase metallicity. The sulphur lines Si II $\lambda \lambda 1250, 1253, 1259 \text{\AA}$ are, however, blended with the intermediate Ly α forest, and Zn II $\lambda \lambda 2026, 2062 \text{\AA}$ show a different velocity profile which may be explained by proximate telluric lines or a blend with an intervening component. However, we only identify an intervening C IV absorber at $z_{\text{abs}} = 2.36$, and a possible Mg II absorber at $z_{\text{abs}} = 2.23$ - none of which will produce strong lines at the position of the Zn II lines. We therefore report the metallicity of the absorbing gas as $[\text{Si}/\text{H}]$. This result is based on two transitions; the mildly saturated Si II $\lambda 1526 \text{\AA}$ line which reveals velocity-structure and broadening-parameters, and the Si II $\lambda 1808 \text{\AA}$ weak line transition to constrain the strength (see Figure 4).

3.2 Quasar point spread function subtraction

To detect the faint stellar continuum of the absorbing galaxy and to search for objects hiding in the bright qPSF, we must isolate the flux from the quasar and subtract it from each image. Traditionally for *HST* images, a PSF is artificially created with TINYTIM, or empirically modelled from bright, unsaturated stars in the same exposure (e.g. Kulkarni et al. 2000; Krogager et al. 2013; Fynbo et al. 2013). The former method is noiseless, can be constructed for the position of the quasar on the detector, and captures the profile of the outer PSF wings. However, the model is limited by the details in its construction; by the accuracy of the recorded telescope aberrations; and can produce unsatisfactory models for saturated objects (e.g. Krogager et al. 2013). The latter method takes advantage of high S/N and is observed simultaneously to the quasar, which mitigates temporal variations. However, it is sensitive to the position of the bright star on the detector plane; to telescope aberrations; is often unable to model the extended PSF wings as the out regions are

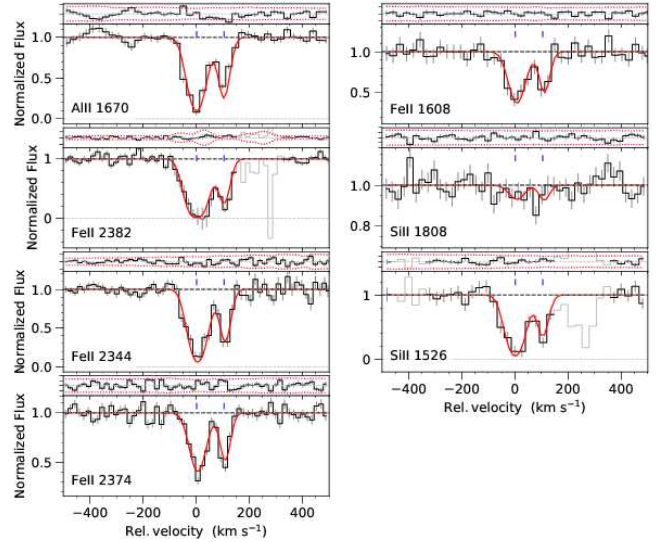


Figure 4. Voigt profile fits to the low-ionisation metal absorption lines of the $z = 2.6775$ DLA towards Q0139-0824. Each panel is subdivided into two sub-panels showing the velocity components of a single transition (bottom), and the fit residuals (top). The black line represents the observed spectrum, with its uncertainties depicted by grey vertical bars in each spectral bin. Grey regions without uncertainties are masked out in the fit. The red curve represents the best fit.

dominated by noise in the sky background; is limited by the number of suitable stars in the field; and there may be a colour mismatch between the object of interest (on our case, the quasar) and stars (Warren et al. 2001).

Since our *HST* programme targeted multiple quasar fields with the same observing strategy, and since the final data products for each filter are drizzled with identical settings (see Section 2.2), the aforementioned caveats can be mitigated by modelling the qPSF from the targeted quasars themselves (e.g. Warren et al. 2001; Augustin et al. 2018). To each i -th quasar, we therefore proceed to construct empirical, non-parametric models of qPSF_i from the median combined stack of all remaining n -th quasar PSFs after rebinning each to a $4\times$ finer grid, and recentering each of these on their respective quasar centroid. Finally, our empirically constructed qPSF_i models are iteratively fitted to their respective quasar, and subtracted from the drizzled science image to search the field for faint stellar continuum emission from the absorber host galaxy (see Figure 5 and Section 3.3), which had previous spectroscopic identifications with emission lines consistent with the DLA redshifts.

In the field of Q 0139–0824, we identify a bright object in the F606W band at low impact parameter. This object clearly overlaps with the quasar PSF, but is unidentified in the other bands. We therefore revisited the quasar spectrum to see whether this object has an absorber counterpart. The spectrum reveals a weak absorber at a redshift $z_{\text{abs}} = 2.233$, which we hypothesise is the counterpart of the bright object. However, the absorption lines are too weak to be compatible with a damped H I absorber, and we therefore leave it to be pursued in future work.

The PSF-subtracted Q 2059–0528 field reveals multiple objects, all of which have larger impact parameters than the limit ($b < 6.3$ kpc) reported in Hartoog et al. (2015). We note, however, that this limit is based on the assumption that the individual Ly α signals in the three slits are detecting the same counterpart.

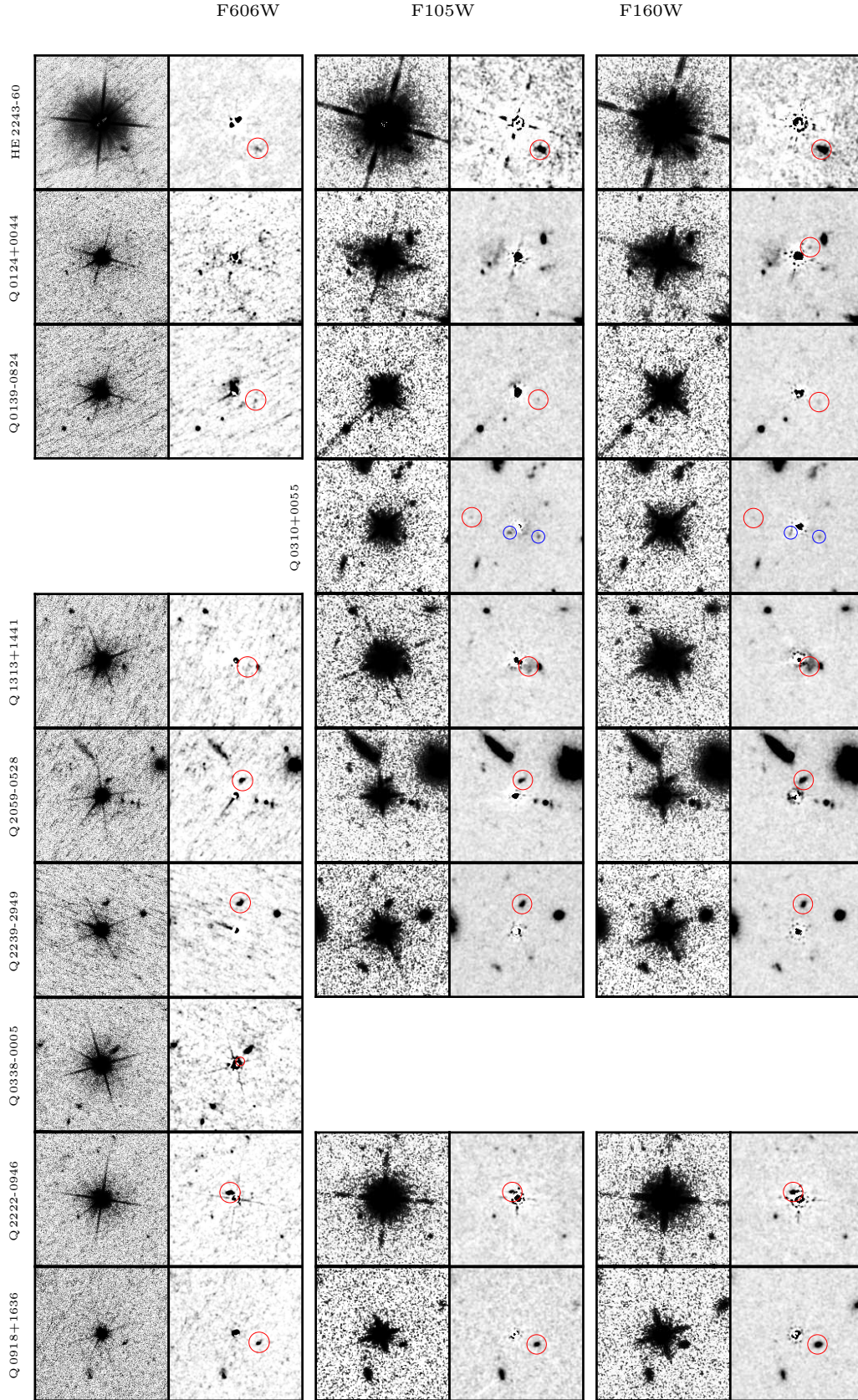


Figure 5. Mosaic of 11×11 arcsec quasar fields. Rows label individual fields. Column doublets label *HST* filters. Each doublet displays the science image (*left*) and qPSF subtracted residual image (*right*) with confirmed detections (red circles) and proximate candidates, in projection, lacking redshift information (blue circles). Each panel is aligned North up East left. For clarity, science images are displayed with a histogram equalisation to enhance faint structures, and residual images have been Gaussian smoothed with a fixed smoothing-length of 0.06 arcsec.

Relaxing this assumption, we note that their reported detection in the PA = -60° slit is the only detection formally above 3σ significance. We therefore identify the bright object immediately North-West of the quasar as the most likely source of the Ly α emission, and as a candidate counterpart to the DLA, and based on that report our results in Table 4. Such a configuration with several components seen in emission appears similar to the DLA host galaxy system towards Q2206–1958, which was shown to be in an active stage of merger (Møller et al. 2002; Weatherley et al. 2005).

3.3 Modelling surface brightness profiles with GALFIT

Having identified the continuum emission counterparts in each quasar-subtracted field, we employ GALFIT (Peng et al. 2002) to model their surface brightness profiles. Here, we do so by iteratively adding Sérsic components which GALFIT implicitly convolve with the PSF-model, and which are fitted simultaneously with the quasar until the galaxy emission is fully captured.

GALFIT has been used to derive structural parameters and magnitudes for individual DLA galaxies in the past (e.g. Krogager et al. 2013; Fynbo et al. 2013; Augustin et al. 2018). We here make an effort to outline and emphasise certain aspects of the fitting procedure which differ for our particular science case, relative to standard retrieval of parameters for a galaxy on a flat sky background.

- Its brightness causes the quasar PSF profile to extend far into the field. It is therefore essential to use a large PSF model, capable of subtracting the flux in the PSF wings. If the PSF does not account for this, GALFIT will overestimate the sky background.
- The large PSF model necessitates a large fitting region. We found that a fitting region of 800×800 pixels for a pixel scale of $0.067 \text{ arcsec pixel}^{-1}$ was needed to ensure robust quasar magnitudes matching known SDSS optical photometry.
- The Sérsic function associates higher (central) light concentrations with larger extended wings. Any over/under estimation of either the sky background and/or the quasar PSF wing will therefore be compensated for by (wrongfully) adjusting the Sérsic index. This will minimise the χ^2 statistic at the expense of unrealistically large concentrations. It is therefore essential to fit the galaxy and quasar simultaneously, and determine the background independently. This is particularly important as our objects lie at small impact parameters, and recognising the brightness contrast between the quasar and the galaxy, a small change in the quasar magnitude may generate large differences in final galaxy parameter estimates.

We therefore fix the sky value to independent measurements determined from the mean of the pixel counts in sky regions free of sources and hot pixels. The zero-point (ZP) for each filter was calculated with the PHOTPLAM and the PHOTFLAM FITS header keywords, with values of $ZP_{F606W} = 26.104$; $ZP_{F105W} = 26.270$; and $ZP_{F160W} = 25.947$. Finally, we input the science image in the recommended units of counts. This is particularly relevant for our science case, as the brightness contrast between the quasar and the galaxy causes pixel values to span a large dynamic range.

We find that adopting a single Sérsic component does not capture the clumpy light distribution observed in many of the objects, and indeed results in large residuals. This behaviour is also reflected in the GALFIT solution, which under such conditions (or for faint objects) becomes unstable to perturbations in initial parameter guesses. We found that iteratively adding components, which collectively capture the effective light distribution of the source, stabilises the parameter range within physically acceptable Sérsic indices ($0.5 \leq n \leq 8$) and effective radii $0.2 \leq r_{\text{eff}}$ [pixels] ≤ 20 ,

although the international distribution of the parameters are sensitive to the initial guesses giving near-identical χ^2 -statistics for different combinations. The final fits suggest that $\sim 40\%$ of absorption-selected galaxies at redshift $z \sim 2-3$ require multiple Sérsic profiles to mitigate apparent systematic residuals and accurately capture the light distribution (for individual number of Sérsic components employed in each fit, see Table 4). We note that the number of Sérsic profiles employed for each host galaxy should be considered lower limits, as they correlate with spatial resolution. However, the fact that 40% reveal multiple star-forming clumps at a drizzled F160W spatial resolution of 0.067 arcsec/pxl at $z \sim 2-3$ agrees with the general trend of clumpy morphologies of high-redshift galaxies Livermore et al. (2015).

Previous studies, often motivated by observational considerations, choose to report structural parameters and morphology based on the band with the highest resolution. Here, we attempt a physically motivated approach, and report morphologies based on the reddest (F160W) band in order to capture the main stellar component. We then fix the morphology in the remaining bands to that derived in F160W, appropriately scaled and rotated to the resolution, pixel sampling and orientation of individual frames.

In order to systematically analyse and compare objects fitted with a single Sérsic profile to those that require multiple components, we therefore take a conservative approach and report non-parametric half-light radii ($r_{1/2}$) calculated from growth curves originating at the luminosity centre of the final galaxy-model; and total (summed over individual Sérsic components) magnitudes (mag_{AB}). For $r_{1/2}$ the final uncertainty reflects a weighted sum of the relative uncertainties from each component contributing to the model. We estimate the magnitude error directly from the quasar+galaxy subtracted residual image as $\Delta F = \sqrt{\sum_{i \in A} \sigma_{\text{tot},i}^2}$, where A is the non-masked pixels in a circular aperture at the position of the galaxy-model luminosity centre with radius $5 \times r_{1/2}$, and $\sigma_{\text{tot},i}$ is the flux count in pixel i . These results are recorded in Table 4.

3.4 Modelling the spectral energy distribution

We determine the stellar mass content ($M_\star (M_\odot)$) in each of the absorbing galaxies by fixing the redshift to the spectroscopic value, and iteratively match SED templates to broad-band magnitudes corrected for Galactic extinction. We use standard Bruzual & Charlot (2003, BC03) simple stellar population (SSP) spectral templates based on Padova 1994 stellar evolutionary tracks and a Chabrier (2003) IMF. We employ the LePhare code (Arnouts et al. 1999; Ilbert et al. 2006), which evaluates the template fit by minimising the χ^2 -statistic across a user pre-defined grid of parameters. Our grid encompasses (i) ages limited to be in the range $0-4$ Gyrs which corresponds to the age of the Universe at the lowest absorption-redshift in our sample; (ii) e-folding time-scales in the range $0.1-30$ Gyrs for the star formation histories; (iii) a Calzetti et al. (2000) attenuation-curve as we are probing redshifts around the peak of cosmic star-formation; (iv) a set of intrinsic colour excesses, E_{B-V} in the range $0-0.3$, sampled in steps of 0.05 and extended if needed to ensure that the preferred E_{B-V} value is associated with χ^2 -minima rather than a grid-boundary. The resulting SED fits of the absorbing galaxies are shown in Figure 6. The stellar masses and their associated measurement uncertainty are determined based on the median, 16th- and 84th percentile from a maximum likelihood analysis of the SED-fits χ^2 distribution, and reported in Table 4. Best fit SFRs, stellar masses and colour excess are reported in Table 5.

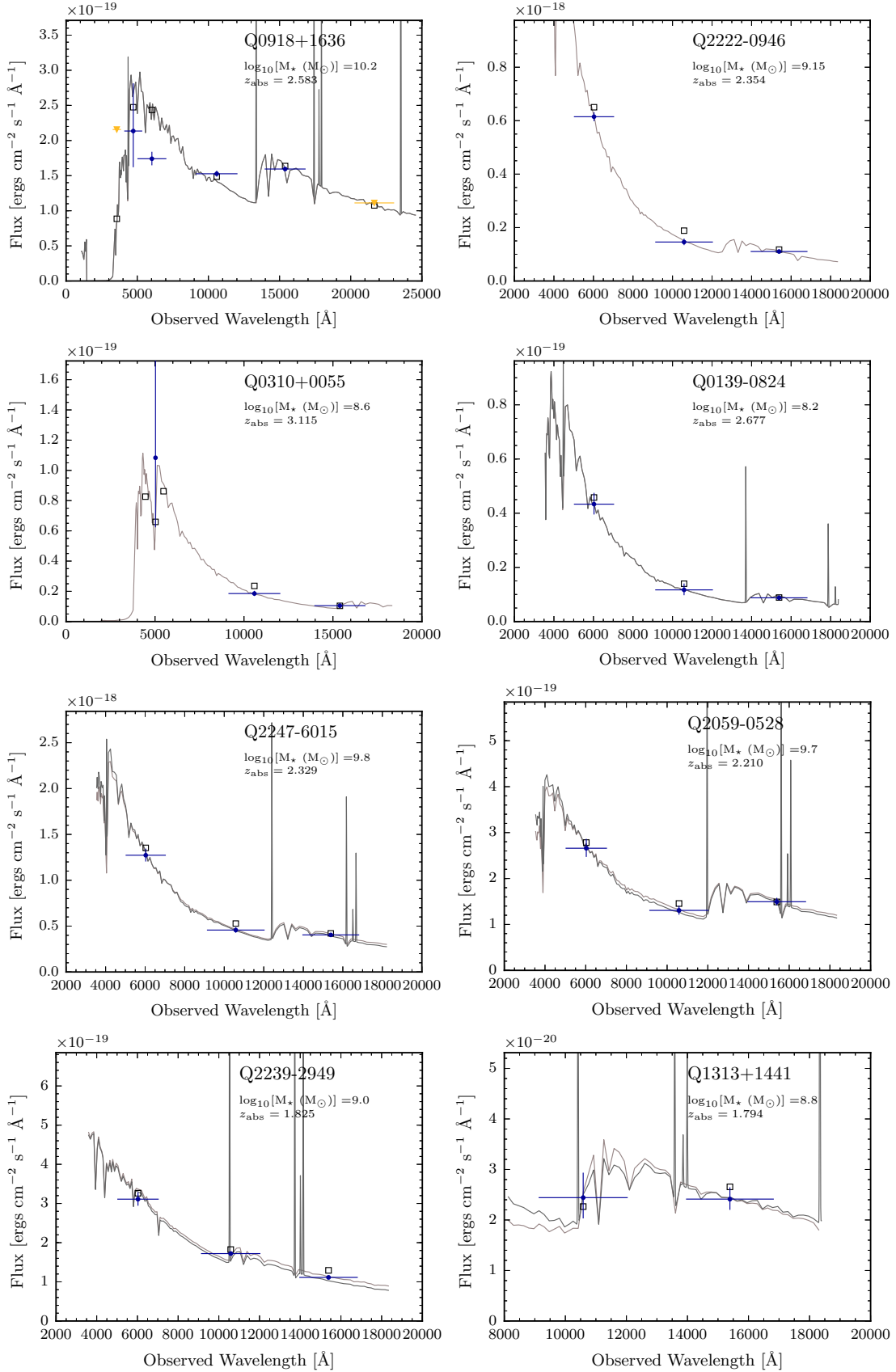


Figure 6. Spectral energy distribution fits minimising the χ^2 -statistic for each absorption-selected galaxy. Blue (yellow) filled symbols refer to included measurements (limits), with vertical and horizontal error-bars indicating magnitude uncertainties and the $FWHM$ of each filter, respectively. Grey empty squares refer to the predicted transmission-weighted flux in each filter, calculated from the best-fit model. Each panel text displays the Object name and resulting stellar mass.

Quasar Field	N_S	P.A. [Deg.]	θ [arcsec]	b [kpc]	$r_{1/2}$ [kpc]	mag _{F606W} [AB]	mag _{F105W} [AB]	mag _{F160W} [AB]
Q0124+0044	1	311 ± 1	1.25 ± 0.04	10.5 ± 0.3	0.4 ± 3.1	-	-	26.9 ± 0.2
Q0139-0824	1	244.6 ± 0.7	1.83 ± 0.03	14.8 ± 0.2	0.4 ± 1.5	27.2 ± 0.1	27.3 ± 0.2	26.8 ± 0.1
Q0310+0055	1	77.9 ± 0.5	3.77 ± 0.04	29.4 ± 0.3	0.5 ± 0.9	-	26.9 ± 0.1	26.7 ± 0.1
Q1313+1441	2	241 ± 2	1.20 ± 0.04	10.3 ± 0.4	2.2 ± 0.7	-	26.5 ± 0.2	25.7 ± 0.1
Q2059-0528	2	334.8 ± 0.3	1.43 ± 0.01	12.05 ± 0.09	1.7 ± 0.3	25.23 ± 0.08	24.71 ± 0.08	23.74 ± 0.06
Q2239-2949	3	348.8 ± 0.7	2.31 ± 0.03	19.8 ± 0.3	1.5 ± 0.4	25.00 ± 0.06	24.39 ± 0.03	24.05 ± 0.03
Q2247-6015	2	222.3 ± 0.3	2.99 ± 0.02	25.0 ± 0.2	2.6 ± 0.3	23.48 ± 0.06	23.33 ± 0.07	22.65 ± 0.04
Q0338-0005	1	305 ± 2	0.39 ± 0.02	3.3 ± 0.2	$1.5^* \pm 0.1$	$25.7^* \pm 0.1$	-	-
Q2222-0946	1	41.1 ± 0.2	0.74 ± 0.01	6.17 ± 0.02	0.52 ± 0.03	24.32 ± 0.03	24.59 ± 0.09	23.63 ± 0.06
Q0918+1636	1	245.78 ± 0.06	2.00 ± 0.01	16.37 ± 0.02	0.81 ± 0.03	25.65 ± 0.06	24.53 ± 0.03	23.66 ± 0.01

Table 4. Results of GALFIT and LePhare modelling of absorber counterparts. N_S refers to the number of Sérsic components employed in the final fit. The Position Angle (P.A.) of the galaxy position relative to that of the quasar, is measured in degrees East of North. The spectroscopically inferred projected angular separation (θ) and associated impact parameter (b) reported in Table 2 have here been replaced by the values measured directly in the *HST* images. Half-light radii, $r_{1/2}$, have been converted from image pixels to physical units of kpc with the drizzled pixel-scale and absorber redshift for the assumed cosmology. Magnitudes are direct measurements not corrected for Galactic extinction. *The effective radius and the associated F606W magnitude of the object identified as the counterpart in the Q0338-0005 field required highly fine-tuned GALFIT setup, and these values should therefore be treated with caution.

Quasar Field	E_{B-V}	$\log_{10}(\text{SFR})$ [$\log_{10}(\text{M}_{\odot} \text{ yr}^{-1})$]	$\log_{10}(\text{M}_{\star})$ [$\log_{10}(\text{M}_{\odot})$]
Q0124+0044	-	-	-
Q0139-0824	0.00	0.05 ± 0.3	8.2 ± 0.2
Q0310+0055	0.00	0.4 ± 0.3	8.6 ± 0.3
Q1313+1441	0.05	$-0.06^{+0.5}_{-0.3}$	$8.8^{+0.3}_{-0.8}$
Q2059-0528	0.20	$1.2^{+0.3}_{-0.4}$	$9.7^{+0.6}_{-0.5}$
Q2239-2949	0.35	1.7 ± 0.2	9.0 ± 0.1
Q2247-6015	0.10	1.6 ± 0.3	$9.8^{+0.7}_{-0.6}$
Q0338-0005	-	-	-
Q2222-0946	0.00	$0.9^{+0.2}_{-0.1}$	$9.15^{+0.09}_{-0.10}$
Q0918+1636	0.25	$1.3^{+0.1}_{-0.2}$	$10.2^{+0.1}_{-0.2}$

Table 5. Results of LePhare modelling of absorber counterparts. The reported E_{B-V} values are the grid-points (sampled at 0.05 step intervals) which minimised the χ^2 statistic. $\log_{10}(\text{SFR})$ and $\log_{10}(\text{M}_{\star})$ are reported as the median values with 1σ errors, determined using LePhare’s built-in maximum likelihood routine. All values are based on the SED fit including the nebulae emission lines apart from Q2222-0946, Q0310+0055 for which information on spectroscopic emission-line fluxes was leveraged to isolate the stellar continuum.

All values are based on the SED fit including the nebulae emission lines apart from Q 2222-0946 and Q 0310+0055, for which information on spectroscopic emission-line fluxes was leveraged to isolate the stellar continuum. For completeness, we also overplot the best-fit SEDs solved for using the same grid, absent emission lines, allowing the reader to assess the impact of the nebulae emission on the derived stellar masses. In the case of Q 2222-0946, we also correct the F160W broadband magnitude for a 33% nebular emission-line contribution, as determined in Krogager et al. (2013).

The magnitude measurements ($\mu_1 \pm \sigma_1$) reported for Q 0918+1636 in Table 4 appear to be in tension with those ($\mu_2 \pm \sigma_2$) reported in Fynbo et al. (2013, their Table 2). We note that whereas our values refer to the direct measurements, the latter have been corrected for Galactic extinction. By applying the relevant extinction corrections reported in Section 2.3, we find that all magnitudes are consistent within the respective uncertainties, with a statistical tension of $(\mu_1 - \mu_2)/\sqrt{\sigma_1^2 + \sigma_2^2} \lesssim 1\sigma$.

4 DISCUSSION

Our sample lies at a mean redshift of $z_{\text{abs}} = 2.3$, with a redshift spread of 0.4. In Figure 7 we show how our sample of absorption selected galaxies falls on the established mass-size relation (*left*), and the main sequence for star-forming galaxies (*right*), both constructed from luminosity-selections and matching our sample in redshift.

To analyse the high-redshift galaxy stellar-mass-size relation, van der Wel et al. (2014) investigate early- and late-type galaxies from the 3D-*HST*-CANDELS survey that are separated by colour-selections and with masses derived for a Chabrier initial mass function (Chabrier 2003). Luminosity-selected samples have size measurements with effective radii corresponding to their semi-major axis from Sérsic models, within averages measured in stellar mass bins. Figure 7 illustrates the relations by the red and blue lines, which presents early- and late-type galaxies at $\langle z \rangle = 2.25$ (van der Wel et al. 2014), with an extrapolation below the reported completeness limits by indicated by the dashed lines. The transparent boxes represent the stellar-mass binned statistics (mean and 1σ dispersion) of circularised r_{eff} , which in definition more closely resemble our non-parametric measurements of the half-light radii.

We fit the Mass-Size relation of the DLA galaxy data with a power-law profile including a term for the intrinsic scatter, and taking into account asymmetric uncertainties in $\log M_{\star}$ and measured radii. The best fit is $\log r_{1/2} = (-0.54^{+1.50}_{-1.65}) + (0.07^{+0.16}_{-0.17}) \log_{10} M_{\star}$, with an internal scatter of $\sigma_{\log r_{1/2}} = 0.26$ dex for the relation. In Figure 7, the best fit curve for DLA galaxies lies closer to the relation traced by late-type (blue) rather than the early-type (red) curves. Specifically, we find that our data are inconsistent with the blue curve with a $\chi^2 = 9.5$ and inconsistent with the red curve with a $\chi^2 = 70$ for eight degrees of freedom. This means DLA galaxies mass-size relation is consistent with the relation from late-type galaxies alone with a probability of $P = 30\%$ or $P \sim 10^{-9}\%$ from that of early type galaxies alone.

Albeit limited by sample size and individual measurement uncertainties, our absorption-selected sample lies on the luminosity-selected relations, and displays a clear preference for the relation traced by late-type galaxies at $z \sim 2$. This result is consistent with the notion that identifying galaxies in absorption preferentially selects less evolved, gas-rich galaxies. In addition, it is remarkable that $\sim 50\%$ of our sample has stellar masses below the formal completeness

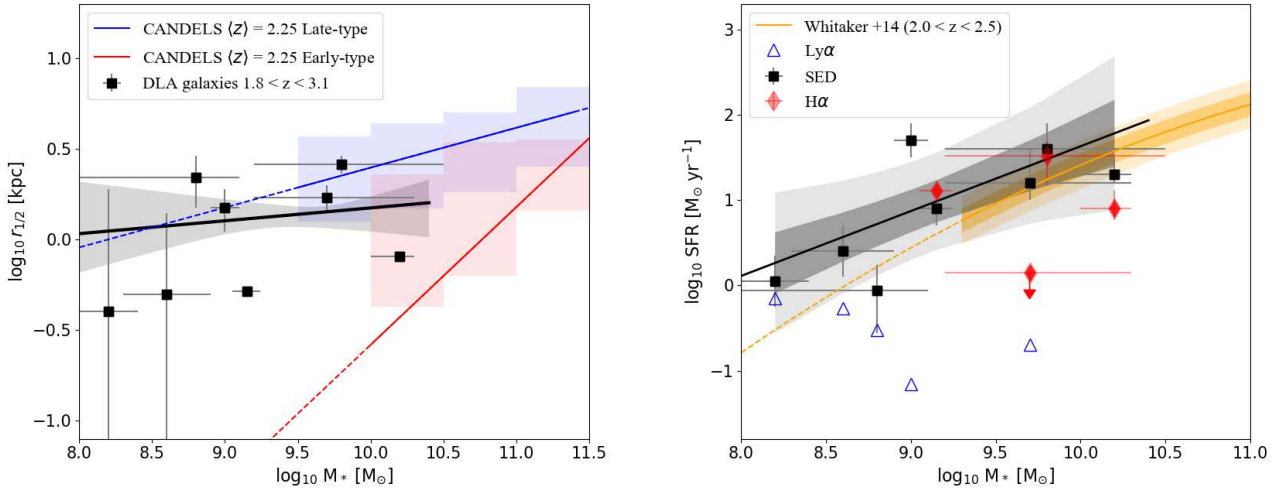


Figure 7. Our $z \sim 2.3$ *HST* sample of absorption selected galaxies placed on scaling relations derived from luminosity-selected samples. *Left:* the mass-size relation for early-type (red) and late-type (blue) galaxies in [van der Wel et al. \(2014\)](#). Lines reflect the relations derived from effective radii measured along the major axis, with dashed segments illustrating an extrapolation beyond the reported completeness limits. The shaded, transparent regions depict mass-binned statistics of the mean and 1σ intrinsic scatter in circularised radii, whose definition is closer to our half-light radii measurements. The DLA galaxies represent preferentially the star-forming population, with an extension to lower mass galaxies. *Right:* the main sequence of star forming galaxies (black line), with 1σ and 2σ confidence intervals as shaded regions, and extrapolation illustrated as dashed segment.

limit for luminosity-selected surveys. It is encouraging to see that even towards the low mass end, our galaxies fall on the extrapolated luminosity-selected mass-size relation and provides direct evidence that absorption selection extends the parameter space towards lower masses at the faint end of high-redshift galaxy luminosity functions.

Having shown that our galaxies have sizes for the derived stellar mass consistent with the luminosity-selected late-type galaxy relation extrapolated to lower masses, we now seek how they lie on the plane spanned by stellar mass and star formation rate. As a reference, we plot the polynomial parametrisation of the main sequence of star-formation for luminosity-selected galaxies at $z \sim 2 - 2.5$ reported in [Whitaker et al. \(2014\)](#), with the associated 1σ - and 2σ scatter in the relation based on the intrinsic dispersion of $\sigma_{\text{intrinsic}} = 0.14$ reported in [Whitaker et al. \(2015\)](#). For our sample, we have incomplete data from three different SFR tracers; lower limits from Ly α ; recombination-line measurements of H α which trace the near-instantaneous SFR on time-scales of ~ 10 Myrs; and SED-based values from LePhare retrieved in the process of deriving stellar masses (see Section 3.4), and constructed to trace the ongoing SFR (see the LePhare package’s documentation). To form a complete census, we plot all the SFR-tracers for each object in Figure 7.

The results of the various diagnostics can be summarised as follows. For objects with SFR measurements in Ly α and either SED or H α , Ly α systematically provide the lowest SFR measurements, in perfect agreement with our expectations based on its resonance nature and effects on inferred SFRs. Therefore, SFRs based on Ly α should only be treated as lower limits. In addition, and considering the limited number of photometric bands available to perform our SED fits, we find a remarkable agreement between H α and SED based SFRs when these are available. Indeed, these results suggest that our galaxies fall perfectly on the predicted main sequence of star forming galaxies.

Since the SED based SFRs are found for all DLA galaxies,

we use this tracer to investigate the scaling relation. A fit to the mass-SFR_{SED} relation for the DLA galaxies using an orthogonal linear regression method with asymmetric uncertainties gives $\log_{10} \text{SFR}_{\text{SED}} = (0.77 \pm 0.58) \log_{10} M_* - (5.99 \pm 5.35)$ with a covariance of -2.19 . The mass-SFR relation at $2.0 < z < 2.5$ in [Whitaker et al. \(2014\)](#) suggests a linear relation with a slope of unity at lower stellar masses, however this is based on an extrapolation below the mass completeness limit.

In the context of absorbing galaxies in general, the fact that our sample so finely trace known scaling relations is interesting in particular, considering their sub-main sequence star forming analogues at $z \sim 0.7$ ([Møller et al. 2018](#); [Kanevar et al. 2018](#); [Rhodin et al. 2018](#)). Unfortunately, our $z \sim 2.3$ *HST* sample does not capture the high end of stellar mass range covered by the low redshift sample and luminosity-selected relations. This inhibits us from discriminating whether sub-main -sequence star-formation is inherent to the selection; related to galaxy evolution; or related to a typical stellar mass-scale $\log_{10}[M_*(M_\odot)] \gtrsim 10$.

5 CONCLUSIONS

In this work, we have performed a systematic analysis based on multi-band high spatial resolution *HST* imaging of a sample of $z \sim 2 - 3$ high column density H I absorption-selected galaxies. The sample consists of seven new and three re-analysed quasar fields, homogeneously selected based on the presence of spectroscopically confirmed galaxy counterparts to metal-rich H I absorbers in the quasar spectra. With the high-resolution imaging data we systematically characterise morphologies and physical quantities of these galaxies. Using quasar absorption as a method of selection, we probe the faint-end of the galaxy luminosity distribution, and characterise in detail a population of star-forming galaxies that are not included in deep luminosity selected high-redshift galaxy studies.

We report on the previously un-published absorption-line analysis of the DLA towards Q0139–0824; and the spectroscopic X-shooter and FORS1 detections of emission from galaxy counterparts to the absorbers towards Q0139–0824 and Q0124+0044. We report on a new photometric F606W detection of the counterpart in the re-analysed quasar field Q0338–0005.

After careful removal of the quasar PSFs, each absorbing galaxy is modelled with Sérsic-profile components to describe the light distribution. The photometric detection of the galaxy counterpart allows us to derive accurate and precise impact parameters and position angles for all systems. From the final galaxy models we derive broad-band photometric magnitudes, stellar masses and half-light radii. The main results can be summarised as follows:

- Our sample spans a large range in stellar mass, with $\log_{10}[M_{\star} (M_{\odot})] = 8.2 - 10.2$. Compared to luminosity-selected samples at similar redshifts, the absorption selections probe a broad range of masses. Particularly, our analysis expands the analysis by more than 1 dex lower mass range compared to that examined from large samples of $z \sim 2$ galaxies detected in deep surveys.
- The measured half-light radii, which fall in the range $r_{1/2} = 0.4 - 2.6$ kpc, forms a relation consistent with the mass-size relation of luminosity-selected samples at $z = 2.25$ selected as late-type, star-forming galaxies, again extending the relation by more than 1 dex to lower stellar masses.
- Combined with SFR estimates ($\lesssim 50 M_{\odot} \text{ yr}^{-1}$) based on spectroscopic H α - and SED-based measurements, our sample is consistent with the star forming main sequence derived for luminosity-selected samples at the same redshift.

Based on our extended sample of absorption-selected high-redshift galaxies our results suggest that at redshift 2–3, a gas cross-section selection detects gas-rich, late-type, star forming galaxies. Previously, an analysis of a smaller sample size of strong absorption-selected galaxies revealed that these galaxies are consistent with being sampled at the faint end of the Lyman-break galaxies (Møller et al. 2002). With the addition of derived stellar masses, we have demonstrated that absorption-selected galaxies follow known scaling relations between masses, SFR, and sizes if extrapolated to even lower masses below the completeness limits as derived from pure luminosity selections.

ACKNOWLEDGMENTS

NHPR and LC are supported by the Independent Research Fund Denmark (DFF - 4090–00079). KEH acknowledges support by a Project Grant (162948–051) from The Icelandic Research Fund. FV acknowledges support from the Carlsberg Foundation Research Grant CF18-0388 “Galaxies: Rise and Death” and the Cosmic Dawn Center of Excellence funded by the Danish National Research Foundation under then Grant No. 140.

DATA AVAILABILITY

Based on observations made with the NASA/ESA Hubble Space Telescope, obtained at the Space Telescope Science Institute, which is operated by the Association of Universities for Research in Astronomy, Inc., under NASA contract NAS 5-26555. Data obtained for this article were accessed via <https://archive.stsci.edu/hst/> (Programme ID 12553).

Based on FORS1 and X-Shooter observations collected at the

European Southern Observatory under ESO programme IDs 189.A-0424 and 081.A-0506, accessed via <http://archive.eso.org>.

This research has made use of the SIMBAD database (<http://simbad.u-strasbg.fr/simbad/>), operated at CDS, Strasbourg, France (Wenger et al. 2000). Astropy (Astropy Collaboration et al. 2013), Photutils (Bradley et al. 2016), Matplotlib (Hunter 2007), and Drizzlepac (STSCI Development Team 2012).

REFERENCES

- Abbott T. M., et al., 2000, in Iye M., Moorwood A. F., eds, Proc. SPIE Vol. 4008, Optical and IR Telescope Instrumentation and Detectors. pp 714–719, doi:10.1117/12.395528
- Appenzeller I., et al., 1998, *The Messenger*, **94**, 1
- Arnouts S., Cristiani S., Moscardini L., Matarrese S., Lucchin F., Fontana A., Giallongo E., 1999, *MNRAS*, **310**, 540
- Asplund M., Grevesse N., Sauval A. J., Scott P., 2009, *ARA&A*, **47**, 481
- Astropy Collaboration et al., 2013, *A&A*, **558**, A33
- Augustin R., et al., 2018, *MNRAS*, **478**, 3120
- Bashir W., Zafar T., Khan F. M., Chishtie F., 2019, *New Astronomy*, **66**, 9
- Berg T. A. M., et al., 2016, *MNRAS*, **463**, 3021
- Berry M., Somerville R. S., Gawiser E., Maller A. H., Popping G., Trager S. C., 2016, *MNRAS*, **458**, 531
- Bouché N., et al., 2012, *MNRAS*, **419**, 2
- Bouché N., Murphy M. T., Kacprzak G. G., Péroux C., Contini T., Martin C. L., Dessauges-Zavadsky M., 2013, *Science*, **341**, 50
- Bradley L., et al., 2016, Photutils: Photometry tools, Astrophysics Source Code Library (ascl:1609.011)
- Bruzual G., Charlot S., 2003, *MNRAS*, **344**, 1000
- Calzetti D., Armus L., Bohlin R. C., Kinney A. L., Koornneef J., Storchi-Bergmann T., 2000, *ApJ*, **533**, 682
- Cappetta M., D’Odorico V., Cristiani S., Saitta F., Viel M., 2010, *MNRAS*, **407**, 1290
- Cashman F. H., Kulkarni V. P., Kisieliuss R., Ferland G. J., Bogdanovich P., 2017, *ApJS*, **230**, 8
- Chabrier G., 2003, *PASP*, **115**, 763
- Christensen L., Møller P., Fynbo J. P. U., Zafar T., 2014, *MNRAS*, **445**, 225
- Crighton N. H. M., et al., 2015, *MNRAS*, **452**, 217
- Fynbo J. P. U., Prochaska J. X., Sommer-Larsen J., Dessauges-Zavadsky M., Møller P., 2008, *ApJ*, **683**, 321
- Fynbo J. P. U., et al., 2010, *MNRAS*, **408**, 2128
- Fynbo J. P. U., et al., 2011, *MNRAS*, **413**, 2481
- Fynbo J. P. U., et al., 2013, *MNRAS*, **436**, 361
- Hartoog O. E., Fynbo J. P. U., Kaper L., De Cia A., Bagdonaite J., 2015, *MNRAS*, **447**, 2738
- Hayes M., et al., 2010, *Nature*, **464**, 562
- Hunter J. D., 2007, *Computing In Science & Engineering*, **9**, 90
- Ilbert O., et al., 2006, *A&A*, **457**, 841
- Jorgenson R. A., Wolfe A. M., 2014, *ApJ*, **785**, 16
- Kanekar N., et al., 2018, *ApJ*, **856**, L23
- Kashikawa N., et al., 2002, *PASJ*, **54**, 819
- Kashikawa N., Misawa T., Minowa Y., Okoshi K., Hattori T., Toshikawa J., Ishikawa S., Onoue M., 2014, *ApJ*, **780**, 116
- Kennicutt Robert C. J., 1998, *ARA&A*, **36**, 189
- Komatsu E., et al., 2011, *ApJS*, **192**, 18
- Krogager J.-K., 2018, arXiv e-prints, p. arXiv:1803.01187
- Krogager J.-K., Fynbo J. P. U., Møller P., Ledoux C., Noterdaeme P., Christensen L., Milvang-Jensen B., Sparre M., 2012, *MNRAS*, **424**, L1
- Krogager J.-K., et al., 2013, *MNRAS*, **433**, 3091
- Krogager J.-K., Møller P., Fynbo J. P. U., Noterdaeme P., 2017, *MNRAS*, **469**, 2959
- Kulkarni V. P., Hill J. M., Schneider G., Weymann R. J., Storrie-Lombardi L. J., Rieke M. J., Thompson R. I., Jannuzi B. T., 2000, *ApJ*, **536**, 36
- Laursen P., Razoumov A. O., Sommer-Larsen J., 2009, *ApJ*, **696**, 853
- Le Fèvre O., et al., 2003, in Iye M., Moorwood A. F. M., eds, Proc. SPIE Vol.

- 4841, Instrument Design and Performance for Optical/Infrared Ground-based Telescopes. pp 1670–1681, [doi:10.1117/12.460959](#)
- Livermore R. C., et al., 2015, [MNRAS](#), **450**, 1812
- Lopez S., Reimers D., D’Odorico S., Prochaska J. X., 2002, [A&A](#), **385**, 778
- López S., et al., 2016, [A&A](#), **594**, A91
- Modigliani A., et al., 2010, in *Observatory Operations: Strategies, Processes, and Systems III*. p. 773728, [doi:10.1117/12.857211](#)
- Møller P., Christensen L., 2020, [MNRAS](#), **492**, 4805
- Møller P., Warren S. J., Fall S. M., Fynbo J. U., Jakobsen P., 2002, [ApJ](#), **574**, 51
- Møller P., et al., 2018, [MNRAS](#), **474**, 4039
- Noterdaeme P., Petitjean P., Ledoux C., Srianand R., 2009a, [A&A](#), **505**, 1087
- Noterdaeme P., Petitjean P., Ledoux C., Srianand R., 2009b, [A&A](#), **505**, 1087
- Noterdaeme P., et al., 2012a, [A&A](#), **540**, A63
- Noterdaeme P., et al., 2012b, [A&A](#), **547**, L1
- Peng C. Y., Ho L. C., Impey C. D., Rix H.-W., 2002, [AJ](#), **124**, 266
- Péroux C., Dessauges-Zavadsky M., D’Odorico S., Kim T.-S., McMahon R. G., 2003, [MNRAS](#), **345**, 480
- Péroux C., Bouché N., Kulkarni V. P., York D. G., Vladilo G., 2012, [MNRAS](#), **419**, 3060
- Prochaska J. X., Gawiser E., Wolfe A. M., Castro S., Djorgovski S. G., 2003, [ApJ](#), **595**, L9
- Prochaska J. X., Herbert-Fort S., Wolfe A. M., 2005, [ApJ](#), **635**, 123
- Prochaska J. X., Chen H.-W., Wolfe A. M., Dessauges-Zavadsky M., Bloom J. S., 2008, [ApJ](#), **672**, 59
- Rafelski M., Neeleman M., Fumagalli M., Wolfe A. M., Prochaska J. X., 2014, [ApJ](#), **782**, L29
- Rahmani H., et al., 2016, [MNRAS](#), **463**, 980
- Rhodin N. H. P., Christensen L., Møller P., Zafar T., Fynbo J. P. U., 2018, [A&A](#), **618**, A129
- Richards G. T., et al., 2001, [AJ](#), **121**, 2308
- STSCI Development Team 2012, DrizzlePac: HST image software, Astrophysics Source Code Library (ascl:1212.011)
- Sánchez-Ramírez R., et al., 2016, [MNRAS](#), **456**, 4488
- Schlafly E. F., Finkbeiner D. P., 2011, [ApJ](#), **737**, 103
- Vanden Berk D. E., et al., 2001, [AJ](#), **122**, 549
- Verhamme A., Schaerer D., Atek H., Tapken C., 2008, [A&A](#), **491**, 89
- Vernet J., et al., 2011, [A&A](#), **536**, A105
- Warren S. J., Møller P., Fall S. M., Jakobsen P., 2001, [MNRAS](#), **326**, 759
- Weatherley S. J., Warren S. J., Møller P., Fall S. M., Fynbo J. U., Croom S. M., 2005, [MNRAS](#), **358**, 985
- Wenger M., et al., 2000, [A&AS](#), **143**, 9
- Whitaker K. E., et al., 2014, [ApJ](#), **795**, 104
- Whitaker K. E., et al., 2015, [ApJ](#), **811**, L12
- Wolfe A. M., Turnshek D. A., Smith H. E., Cohen R. D., 1986, [ApJS](#), **61**, 249
- Wolfe A. M., Prochaska J. X., Jorgenson R. A., Rafelski M., 2008, [ApJ](#), **681**, 881
- Zafar T., Popping A., Péroux C., 2013, [A&A](#), **556**, 140
- Zafar T., Péroux C., Popping A., Milliard B., Deharveng J. M., Frank S., 2013, [A&A](#), **556**, 141
- Zafar T., Møller P., Péroux C., Quiret S., Fynbo J. P. U., Ledoux C., Deharveng J.-M., 2017, [MNRAS](#), **465**, 1613
- van der Wel A., et al., 2014, [ApJ](#), **788**, 28

This paper has been typeset from a \LaTeX file prepared by the author.